

The Detectability of Kiloparsec-scale Dual Active Galactic Nuclei: The Impact of Galactic Structure and Black Hole Orbital Properties

Kunyang Li[®], David R. Ballantyne[®], and Tamara Bogdanović[®]
School of Physics and Center for Relativistic Astrophysics, 837 State St NW, Georgia Institute of Technology, Atlanta, GA 30332, USA; kli356@gatech.edu, david.ballantyne@physics.gatech.edu, tamarab@gatech.edu

Received 2021 February 27; revised 2021 May 25; accepted 2021 May 27; published 2021 August 4

Abstract

Observational searches for dual active galactic nuclei (dAGNs) at kiloparsec separations are crucial for understanding the role of galaxy mergers in the evolution of galaxies. In addition, kiloparsec-scale dAGNs may serve as the parent population of merging massive black hole (MBH) binaries, an important source of gravitational waves. We use a semi-analytical model to describe the orbital evolution of unequal mass MBH pairs under the influence of stellar and gaseous dynamical friction in post-merger galaxies. We quantify how the detectability of approximately 40,000 kpc-scale dAGNs depends on the structure of their host galaxies and the orbital properties of the MBH pair. Our models indicate that kiloparsec-scale dAGNs are most likely to be detected in gas-rich post-merger galaxies with smaller stellar bulges and relatively massive, rapidly rotating gas disks. The detectability is also increased in systems with MBHs of comparable masses following low eccentricity prograde orbits. In contrast, dAGNs with retrograde, low eccentricity orbits are some of the least detectable systems among our models. The dAGNs in models in which the accreting MBHs are allowed to exhibit radiative feedback are characterized by a significantly lower overall detectability. The suppression in detectability is most pronounced in gas-rich merger remnant galaxies, where radiation feedback is more likely to arise. If so, then large, relatively gas-poor galaxies may be the best candidates for detecting dAGNs.

Unified Astronomy Thesaurus concepts: Dynamical friction (422); Galaxy evolution (594); Galaxy mergers (608); Supermassive black holes (1663); AGN host galaxies (2017)

1. Introduction

The hierarchical formation model of galaxy evolution predicts that massive galaxies are built up through a series of mergers (e.g., White & Rees 1978; White & Frenk 1991). As the nuclei of most massive galaxies contain a massive black hole (MBH; e.g., Kormendy & Ho 2013), it is expected that many mergers will lead to a remnant with at least two MBHs (e.g., Begelman et al. 1980). Most mergers generate significant nuclear gas flows (e.g., Di Matteo et al. 2005) that provide a favorable environment in which the MBHs can accrete and shine as active galactic nuclei (AGNs). Therefore, a population of dual AGNs (dAGNs) in post-merger galaxies is an unavoidable prediction of hierarchical galaxy formation (e.g., De Rosa et al. 2019). In addition, dAGNs are expected to be the parent population of binary MBHs, where the two MBHs are gravitationally bound and the orbit decays through the emission of gravitational waves (e.g., Begelman et al. 1980; Amaro-Seoane et al. 2017; Kelley et al. 2017, 2019). Thus, understanding the population of dAGNs is necessary for determining the expectations for future gravitational wave experiments.

Observational searches for dAGNs at radio, optical, infrared, and X-ray wavelengths have uncovered only a small number of confirmed systems, especially those with separations <1 kpc (e.g., De Rosa et al. 2019; Foord et al. 2019, 2020; Gross et al. 2019; Hou et al. 2019, 2020; Severgnini et al. 2021). There are two principle difficulties in identifying kiloparsec-scale dAGNs: (1) the small separation of dAGNs (equivalent to \sim 1" at $z \approx$ 0.05), requiring exquisite angular resolution, and (2) significant obscuration (Scoville et al. 1986; Sargent et al. 1987, 1989; Hopkins et al. 2005a, 2012; Narayanan et al. 2008) in the nuclei of post-merger galaxies. As a result, despite significant observational effort, the number of confirmed

kiloparsec-scale dAGN remains very low (<10%) (Burke-Spolaor 2011; Koss et al. 2012; Teng et al. 2012; Mezcua et al. 2014; Fu et al. 2015a, 2015b) with respect to the expectations based on the merger rate of galaxies (Hopkins et al. 2005b; Springel et al. 2005; Van Wassenhove et al. 2012; Capelo et al. 2017), which limits the ability to compare to theoretical models and infer MBH binary merger rates.

Another set of challenges arises from models that attempt to predict the formation and evolution of dAGNs (e.g., Rosas-Guevara et al. 2019). Calculations of dAGN formation in cosmological simulations often lack the resolution needed to calculate the observational properties of the AGNs on kiloparsec or smaller scales. In contrast, simulations of isolated merging galaxies can focus on the timescales and observational properties of an evolving MBH pair in a merger remnant (e.g., Capelo et al. 2017). These simulations are however relatively computationally expensive, and so only a limited number of merger configurations can be explored.

Theoretically, dynamical friction (DF) is expected to dominate the orbital decay of MBH pairs from kiloparsec separations until they are gravitationally bound. In earlier work (Li et al. 2020a, hereafter LBB20a), we deployed a semi-analytical model to study the effects of galactic and orbital parameters on the inspiral time and eccentricity evolution of a secondary MBH due to gaseous and stellar DF at kiloparsec scales. Here, we add a prescription to describe accretion onto both MBHs in our model and consider the observational properties of these dAGNs in ≈40,000 simulations. In particular, we quantify the detectability of each dAGN system as a function of three key parameters: inspiral time, characteristic separation, and characteristic luminosity ratio. By considering how the detectability varies with galaxy (e.g., bulge mass, gas fraction) and orbital properties (e.g., prograde versus retrograde, high versus low

eccentricity), we are able to describe the types of post-merger galaxy remnants that are most likely to host detectable dAGNs.

This paper is organized as follows. Section 2 summarizes the model for orbital evolution of a MBH in the remnant galaxy due to DF and calculation of the AGN luminosities. In Section 3, we describe the probability distribution of dAGN given in terms of their separations and luminosity ratios. Section 4 presents the characteristic luminosity ratios and separations of the model dAGNs and how they depend on the properties of the host galaxy. The calculation of dAGN detectability is also presented in this section. The implications of our results for observational searches for dAGNs are discussed in Section 5, with Section 6 providing the conclusions.

2. Methods

Here, we provide a brief overview of the most important aspects of our model and point the reader to LBB20a for a complete description. We then introduce the method to calculate the accretion rate onto the two MBHs and the emitted luminosity.

2.1. Model of the Remnant Galaxy

We assume that a galaxy merger produces a single remnant, with a stellar bulge and gas and stellar disk, which includes the MBH pair. The primary MBH (pMBH; with mass M_1) is fixed at the center of the galaxy. The nonrotating bulge has a mass $1000 M_1$ (e.g., Magorrian et al. 1998), and follows a power-law density profile that is cutoff at the characteristic outer radius (e.g., Binney & Tremaine 2008). We consider the orbital evolution of a bare, secondary MBH (sMBH; with mass $M_2 < M_1$) under the assumption that it has been stripped of any gas and stars (e.g., Kelley et al. 2017), and is orbiting in the plane of the gas and stellar disks. The total mass of the pair of MBHs is $M_{\rm bin} = M_1 + M_2$ and the mass ratio is $q = M_2/M_1$.

The gas disk in our model has an exponential profile with a scale radius $R_{\rm sd}$ (e.g., Binney & Tremaine 2008). The scale radius of the stellar disk is set to be $\log(M_1/10^5M_{\odot})$ kpc, and that of the gas disk is two times $R_{\rm sd}$. Therefore galaxy models with larger $M_{\rm bin}$ have gas densities that decrease more slowly with radius. The stellar bulge follows a coreless power-law density profile, with the scale parameters also proportional to $\log(M_1/10^5M_{\odot})$ kpc.

The gas and stellar disks rotate together with velocity $v_{\rm g}(r)$, defined in units of local circular velocity $v_{\rm c}(r)$. If the sMBH is co-rotating with the galaxy disks on a prograde orbit, then we assign the disks' velocity as $v_{\rm g} > 0$, whereas in the case of a counter-rotating sMBH the disks' velocity is described as $v_{\rm g} < 0$. The disks are further described by (a) the central gas number density $(n_{\rm gd0})$, which determines the mass of the gas disk within 1 kpc $(M_{\rm gd,1})$, and (b) the gas disk mass fraction $(f_{\rm gd} = M_{\rm gd,1}/(M_{\rm gd,1} + M_{\rm sd,1}))$, where $M_{\rm sd,1}$ is the mass of the stellar disk within 1 kpc. Therefore, each merger remnant galaxy model is defined by five parameters $(M_{\rm bin}, q, n_{\rm gd0}, f_{\rm gd},$ and $v_{\rm g}$), listed in Table 1, which together yield a total of 39,366 model galaxies.

The orbital evolution of the sMBH due to gaseous and stellar DF is followed until the separation between the two MBHs reaches 1 pc, at which point the simulation ends. In order to provide an intuitive description of orbit geometries, we characterize them in terms of the orbital eccentricity (*e*) and

semimajor axis (a). As the orbits of the sMBH in the remnant galaxy are not closed, we use the farthest and closest approaches of the MBHs in each orbit to estimate e and a. With these definitions, each simulation is initialized with $a \sim 1$ kpc and eccentricity e_i . For presentation purposes, we focus on two groups of models: those with low initial eccentricity ($0 \le e_i \le 0.2$) and high initial eccentricity ($0.8 \le e_i \le 0.9$). Thus, the suite of models spans a wide range in initial orbital eccentricity and includes both prograde and retrograde orbits

2.2. DF

The orbital decay of the sMBH in our models occurs due to the combined effect of stellar and gaseous DF. Stellar DF is exerted by both the bulge and the stellar disk and is calculated using Equations (5)–(7) in LBB20a, following the work of Antonini & Merritt (2012). The velocity distribution of stars in the bulge is assumed to be Maxwellian (see Equation (2) in Li et al. 2020b, hereafter LBB20b). We assume that all stars in the stellar disk are rotating with a speed of $v_g(r)$, so that the stellar velocity distribution is a delta function defined at $v_g(r)$. The contribution to the DF force from the stellar disk is negligible relative to the other galaxy components (LBB20a).

As gaseous DF depends on the Mach number of the moving body (e.g., Ostriker 1999; Kim & Kim 2007), the sound speed and thus, the temperature of the gas disk must be defined for each model. We set the temperature profile to be 10^4 K above the minimum temperature required by the Toomre stability criterion (Toomre 1964). This threshold effectively captures shock heating and turbulent energy in the post-merger galaxy (e.g., Barnes & Hernquist 1991). We calculate the gaseous DF force on the sMBH using Equations (10)–(12) of LBB20a, which result in the gaseous DF force that is strongest when the velocity difference between the sMBH and gas disk (Δv) is close to the sound speed, c_s (Kim & Kim 2007).

According to LBB20a, the evolution time $t_{\rm evol}$ (time for the MBHs to reach a separation <1 pc) can range from as short as ~1 Gyr if the stellar bulge dominates the evolution (or if the eccentricity grows large and the sMBH plunges below 1 pc). However, if the gas disk dominates the DF force $t_{\rm evol}$ is more typically ~5 Gyr, but can be as long as \gtrsim 10 Gyr depending on the orbital configuration of the sMBH.

2.3. Calculation of Accretion Rate and Luminosity

The fixed pMBH and the moving sMBH are both allowed to accrete matter from their surroundings and thus, may appear as a dAGN. In the model outlined above, the sMBH may pass through a wide range of environments during its orbital decay, speeding up and slowing down as it sinks into the galaxy. Therefore, its luminosity as an AGN is affected by both its motion and the properties of the host galaxy.

The accretion rates onto both the pMBH and sMBH are calculated in each simulation as a function of time. We describe the accretion rate onto the stationary pMBH using a constant Bondi accretion rate (Bondi & Hoyle 1944; Bondi 1952) that depends only on the central properties of the model galaxy. In addition, we assume the luminosity of the central AGN does not exceed 10% of the Eddington luminosity, in order to match the typical values found in X-ray surveys of AGNs (e.g., Lusso et al. 2012). Specifically, the luminosity of the pMBH is

Table 1Galaxy Model Parameters

Symbol	Definition	Values
$v_{\rm g}(r)$	Gas disk rotational speed in units of $v_c(r)$	$-0.9 \ v_{c}(r),, 0.9 \ v_{c}(r) \ (\text{step} = 0.1 \ v_{c}(r))$
q	MBH mass ratio, M_2/M_1	$1/n \ (n=2,, 9)$
$M_{ m bin}$	Total MBH mass, $M_1 + M_2$	$(2, 3, 5) \times 10^5 M_{\odot}$
		$(1, 3) \times 10^6 M_{\odot}$
		$(1, 3) \times 10^7 M_{\odot}$
		$(1, 3) \times 10^8 M_{\odot}$
$n_{ m gd0}$	Gas number density at the center of galaxy	$100, 200, 300 \mathrm{cm}^{-3}$
$f_{ m gd}$	Gas disk mass fraction, $M_{\rm gd,1}/(M_{\rm gd,1}+M_{\rm sd,1})$	0.3, 0.5, 0.9

Note. $v_g < 0$ ($v_g > 0$) corresponds to the sMBH moving on a retrograde (prograde) orbit relative to the gas and stellar disk. $M_{gd,1}$ and $M_{sd,1}$ are the masses of the gas and stellar disks within a 1 kpc radius, respectively.

determined by

$$L_{1} = \begin{cases} 0.1 \dot{M}_{B1} c^{2} & \text{when } L_{1} < 0.1 L_{1,Edd}, \\ 0.1 L_{1,Edd} & \text{otherwise,} \end{cases}$$
 (1)

where $\dot{M}_{\rm B1} = \pi \ n_{\rm gd0} \ m_{\rm p} (GM_{\rm l})^2 / c_{\rm s1,\infty}^3$ is the Bondi accretion rate of the primary and $L_{\rm l.Edd} = 4\pi G M_{\rm l} m_{\rm p} c / \sigma_{\rm T}$ is the Eddington luminosity of the pMBH. Here, $c_{\rm s1,\infty}$ is the sound speed of the unperturbed gas in the galaxy center, $\sigma_{\rm T}$ is the Thomson cross section, and other constants have their usual meaning.

Accretion onto the sMBH is calculated using the Bondi–Hoyle–Lyttleton (BHL; Hoyle & Lyttleton 1939; Bondi & Hoyle 1944; Bondi 1952) model, where accretion is no longer spherically symmetric since most of the inflow streams past the MBH and is gravitationally focused on the symmetry axis of the moving MBH. A fraction of the gas becomes gravitationally bound to the sMBH and is accreted on it, giving rise to the luminosity

$$L_2 = \begin{cases} 0.1 \dot{M}_{\text{BHL}} c^2 & \text{when } L_2 < L_{2,\text{Edd}}, \\ L_{2,\text{Edd}} & \text{otherwise,} \end{cases}$$
 (2)

where $L_{2,\rm Edd} = 4\pi G M_2 m_{\rm p} c/\sigma_{\rm T}$ is the Eddington luminosity for the sMBH. $\dot{M}_{\rm BHL} = \dot{M}_{\rm B2}/(1+\Delta v^2/c_{\rm s2,\infty}^2)^{3/2}$ is the BHL accretion rate of the secondary, with $\dot{M}_{\rm B2}$ representing the Bondi rate of the sMBH. $c_{\rm s2,\infty}$ refers to the sound speed of the unperturbed gas at the same galactocentric radius as the sMBH and Δv is the velocity of the sMBH relative to the gas disk.

The Δv factor in $\dot{M}_{\rm BHL}$ leads to significant variations as the sMBH evolves through the galaxy (see Appendix for a description of the time-averaged accretion rates). For example, a smaller Δv leads to a higher accretion rate onto the sMBH, and the AGN luminosity will be largest when the velocity of the sMBH is equal to the rotation speed of the galaxy, $v_{\rm g}$. This implies that sMBHs on prograde orbits are more luminous than those on retrograde orbit. However, AGNs on retrograde orbits with large eccentricity can also have large L_2 at the apocenter, where the sMBH has a fairly low Δv . Thus, L_2 is affected by the distribution of gas in the galaxy remnant and can exhibit strong variations due to the orbital evolution of the sMBH.

The calculations described above assume that the MBH masses are constant in time. Similarly, the luminosities L_1 and L_2 are bolometric and do not account for any absorption or extinction within the merger remnant. To minimize the impact of these assumptions hereafter we characterize modeled dAGNs using the luminosity ratio, L_2/L_1 , rather than individual

AGN luminosities. This partly mitigates the impact of neglecting the intragalactic absorption and MBH growth. The impact of these assumptions is discussed in Section 5.2.

3. Characterizing dAGN Properties

Observationally, the ability to successfully identify a kiloparsec-scale dAGN depends on both its separation (d) and luminosity ratio (L_2/L_1), where larger values increase the chance of positive detection. It is therefore important to determine the conditions that could increase the chances of finding dAGNs.

Each of our models produces a description of the dAGN position and luminosity over its evolution time, t_{evol} . In order to determine how the structure of the galaxy and properties of the sMBH orbits affect the evolution of d and L_2/L_1 , we compute the fraction of time that a dAGN spends at certain d and L_2/L_1 . For each of the 39,366 dAGN simulations, we calculate a two-dimensional probability distribution, f_t , by summing the time the dAGN spends at a specific separation d_i and luminosity ratio $(L_2/L_1)_i$

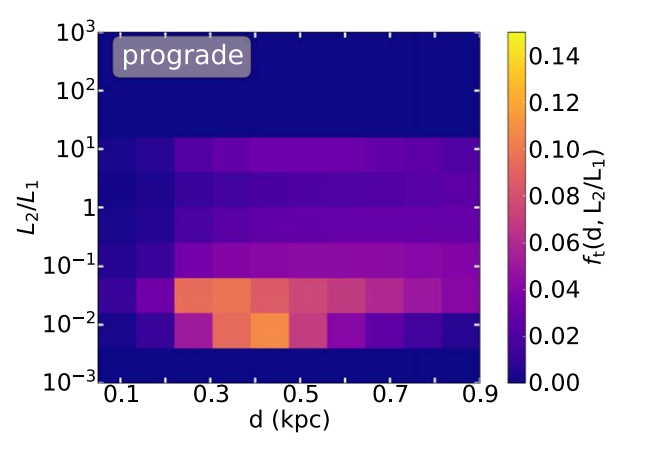
$$f_t[d_i, (L_2/L_1)_j] = \frac{1}{t_{\text{evol}}} \sum_t \Delta t[d_i, (L_2/L_1)_j],$$
 (3)

where i = 1, 2, ..., 9 and j = 1, 2, ..., 6. The range of separations (0, 0.9 kpc) is evenly divided into nine bins with size of 0.1 kpc, while the logarithm of the luminosity ratio (ranging from -3 to 3) is divided into six bins with a size 1. The maximum in the probability distribution occurs where the dAGN spends the largest fraction of time, and is identified as the *most likely* combination of the luminosity ratio and separation at which the dAGN would be observed.

Figures 1 and 2^2 show examples of the probability distributions calculated in this way. In order to build up a signal that better highlights the impact of specific galactic or orbital properties, both panels in the figures shows the sum of f_t over all values of $n_{\rm gd0}$ and $f_{\rm gd}$ while holding the remaining parameters ($M_{\rm bin}$, q, and $v_{\rm g}$) fixed. Figure 1 shows f_t for dAGNs with $M_{\rm bin} = 3 \times 10^6 M_{\odot}$, q = 1/9, and $v_{\rm g} = 0.2 v_{\rm c}$ on prograde and retrograde orbits. The most likely luminosity ratio for dAGNs with these properties is $\sim 10^{-2}$, and the most probable

¹ The separation d used in this paper is the physical distance between the two MBHs and not a projected distance on the sky. For a random distribution of orientations, the average projected separation is $(\pi/4)d$.

² See our Github page for the code and data for generating two-dimensional probability distribution of dAGNs: https://github.com/kli356/Dual-AGN-Detectability.



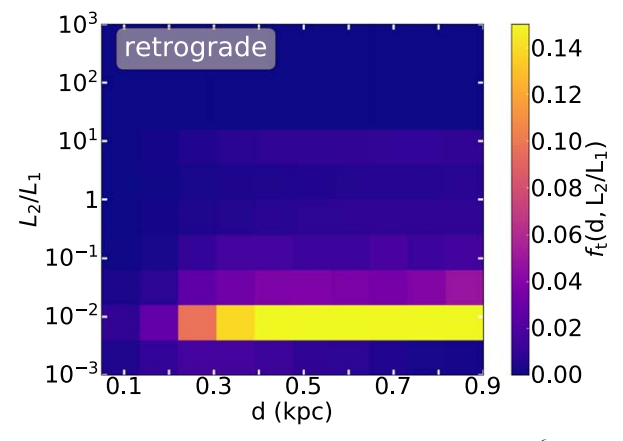
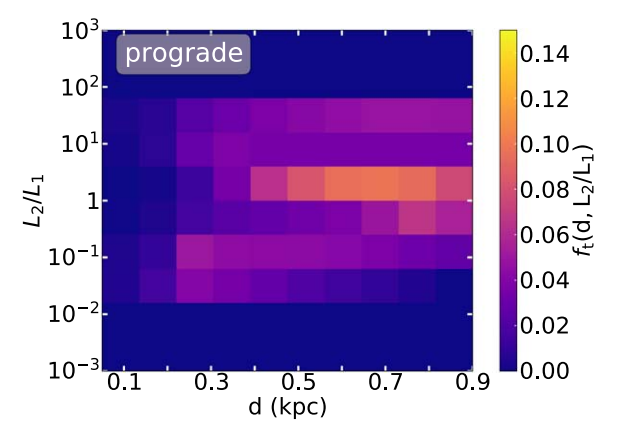


Figure 1. The two-dimensional probability distribution of dAGNs on prograde (left panel) and retrograde orbits (right) in galaxies with $M_{\rm bin} = 3 \times 10^6 \, M_{\odot}$, q = 1/9, and $v_{\rm g} = 0.2 v_{\rm c}$. The distributions are summed over all values of $n_{\rm gd0}$ and $f_{\rm gd}$. The color bars mark the value of the probability.



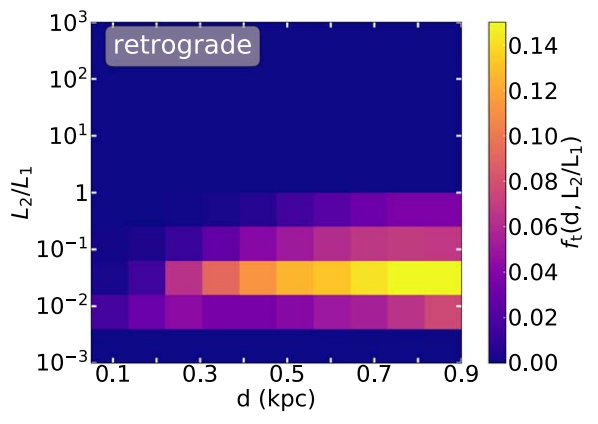


Figure 2. Similar to Figure 1, but for dAGNs with $M_{\rm bin} = 10^8 M_{\odot}$, q = 1/3, and $v_{\rm g} = 0.8 v_{\rm c}$.

dAGN separation is $d \sim 0.3$ –0.4 kpc for prograde and $d \sim 0.4$ –0.9 kpc for retrograde orbits. This difference between the prograde and retrograde orbits is a natural consequence of the effect of gaseous DF. Due to the direction of gas DF at the apocenter of orbits, the eccentric prograde orbits decreases in eccentricity while moving through gas disks, while eccentric retrograde orbits become increasingly more eccentric. Therefore, eccentric prograde orbits tend to be circularized shortly after the start of the simulation, hence the separation between the two MBHs do not vary significantly during one orbit of evolution. However, the growth in eccentricity of eccentric retrograde orbits makes the variation of separation per orbit larger, which results in a wider range of potentially observed separations than that in eccentric prograde orbits (see LBB20a for details).

Figure 2 shows f_t for dAGNs in more massive and rapidly rotating galaxies, containing comparable mass MBH pairs $(M_{\rm bin}=10^8~M_{\odot},~v_{\rm g}=0.8v_{\rm c},~{\rm and}~q=1/3)$. Galaxies with these properties host dAGNs with larger L_2/L_1 than those featured in Figure 1. The higher luminosity ratio is due to the smaller relative velocity between the sMBH and the rotating gas disk. Lower Δv boosts the BHL accretion rate onto sMBH and increases its luminosity. Similarly, in our model, more massive pMBHs reside in more massive and extended gas disks (Section 2.1), causing sMBHs in such systems to experience larger gas densities (and consequently accretion luminosities) throughout their orbit. Larger q values have a similar effect on the accretion rate due to the more massive sMBHs. Figure 2 also indicates that the most likely dAGN separations are larger

for MBH pairs in massive galaxies than for systems shown in the previous figure. This is a direct consequence of the rate of evolution of these systems, which is relatively slow at large separations (where their evolution is gas disk dominated) and faster at smaller separation (where it is bulge dominated). Note that this trend is also present for lower mass galaxies shown in Figure 1 but that their smaller physical size implies smaller separations for dAGNs. Both Figures 1 and 2 indicate that the probability of detection of dAGNs will depend on the type of galaxy in which the system resides and the nature of the orbit of the sMBH.

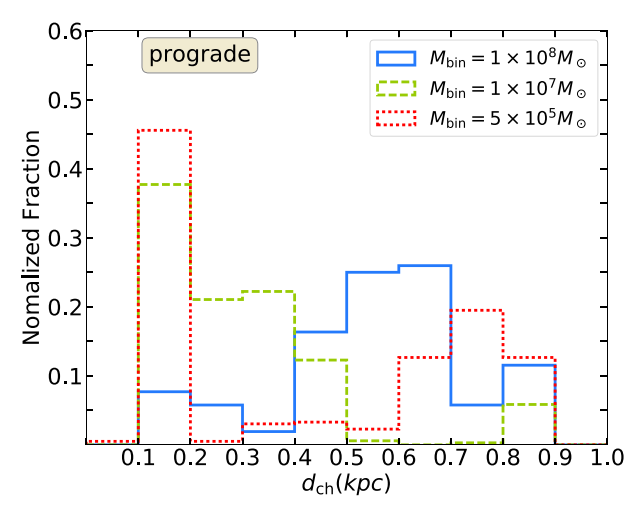
4. The Effect of Galactic and Orbital Properties on the Characteristics of dAGNs

To determine how galaxy properties affect the most probable dAGN luminosity ratios and separations we sum the twodimensional probability distributions described in the previous section along one of their axes. For example, the probability distribution for (L_2/L_1) is

$$g_t[(L_2/L_1)_j] = \sum_i f_t[d_i, (L_2/L_1)_j].$$
 (4)

The most probable luminosity ratio for dAGNs is given by the peak of this distribution. We thus define this maximum to be the characteristic luminosity ratio, $(L_2/L_1)_{ch}$, for a particular class of dAGNs with common properties,

$$g_t[(L_2/L_1)_{ch}] = \max[g_t[(L_2/L_1)_i]].$$
 (5)



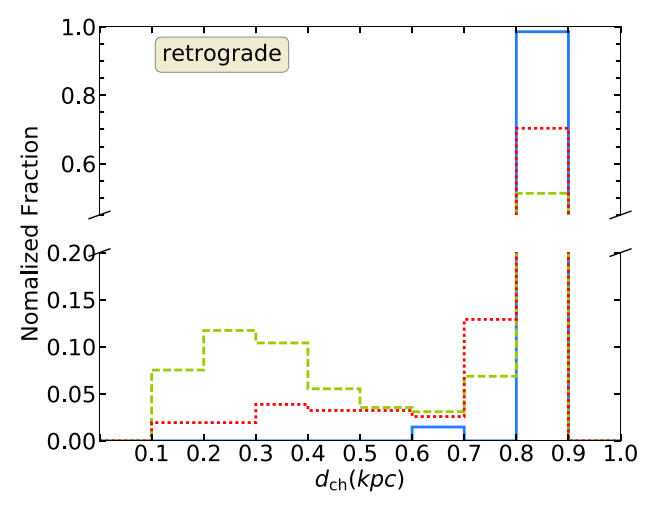


Figure 3. Histograms of the characteristic (most probable) dAGN separation, d_{ch} for sMBHs on prograde (left), and retrograde (right) orbits and systems with different M_{bin} .

Similarly, the characteristic separation of a dAGN, $d_{\rm ch}$, is defined as

$$g_t(d_{ch}) = \max [g_t(d_i)], \tag{6}$$

where $g_t(d_i)$ is the one-dimensional probability distribution calculated using an expression analogous to Equation (4). We use these expressions to compute values of $(L_2/L_1)_{\rm ch}$ and $d_{\rm ch}$ for all dAGNs in our model suite.

4.1. dAGN Separation

dAGNs are easiest to spatially resolve when they are widely separated on the sky. It is therefore important to understand which galaxy properties and orbital configurations increase the chances of observing a dAGN with a large separation. Figure 3 shows histograms of the characteristic dAGN separations for different values of $M_{\rm bin}$, as well as the prograde or retrograde sMBH orbits. It illustrates that sMBHs on prograde orbits have smaller separations than those on retrograde orbits, on average. This is because the sMBH on prograde orbits tend to circularize, even if they started on eccentric orbits, whereas those on retrograde orbits tend to grow more eccentric (LBB20a). As a result, retrograde sMBHs are more likely to be observed with large, approximately kiloparsec separations.

Another important parameter that affects the distribution of $d_{\rm ch}$ is $M_{\rm bin}$. Regardless of the sense of rotation of the sMBH, the pairs with larger $M_{\rm bin}$ have larger characteristic separations, particularly for prograde orbits. This can be understood because the mass and size of the bulge, as well as the gas and stellar disk of the remnant galaxy, are proportional to M_1 (see Section 2.1). Thus, increasing $M_{\rm bin}$ for a fixed value of M_2 implies higher gas and stellar density at a given radius in the remnant galaxy, and consequently, faster orbital evolution of the sMBH. This means that the characteristic separation where dAGNs spend a significant fraction of their time, and are likely to be observed, moves outward (toward larger values of $d_{\rm ch}$) with increasing $M_{\rm bin}$.

We also examine the distribution of $d_{\rm ch}$ as a function of the rotation speed of the galactic disk and show results in Figure 4. This is relevant because the magnitude of the DF force directly depends on the relative velocity between the sMBH and the rotating gas disk through which the MBH is moving (see Section 2.2). For MBHs on prograde, and in general eccentric

orbits, the cumulative effect of the gas DF force is largest at the apocenter, where the sMBH spends the largest fraction of its orbital period. For slowly rotating gas disks (i.e., $v_g = 0.2 v_c$), the relative velocity at the apocenter for sMBHs on moderately eccentric orbits leads to increased efficiency of gaseous DF. Consequently, these orbits evolve quickly on average, and their dAGNs are most likely be observed with smaller separations, as illustrated in Figure 4. As v_g increases, the gaseous DF force acting on prograde sMBHs with moderate eccentricity at their apocenter diminishes. As a result, dAGNs in rapidly rotating galaxies evolve more slowly and are more likely to be observed with $d_{\rm ch} \sim 0.7$ kpc. When it comes to sMBHs on retrograde orbits, the relative velocity between the secondaries and their galactic gas disks is always large, and hence, these dAGNs are likely to be observed with large separations ($d_{\rm ch} \sim$ 0.8–0.9 kpc), as shown in the right panel of Figure 4.

In summary, for the sMBH on a prograde orbit, the most likely dAGN separation can be as low as \sim 0.1 kpc, especially if the merger galaxy is rotating slowly or has a low mass. We expect dAGN separations with the sMBH on a retrograde orbit to be $d_{\rm ch} \sim 0.8$ kpc, for a wide range of remnant galaxy properties. We also find that other properties of the merger remnant galaxies (e.g., $n_{\rm gd0}$) or MBH pairs (e.g., q) do not significantly affect the distribution of $d_{\rm ch}$.

4.2. Luminosity Ratios of dAGNs

In this section we discuss the distribution of the most likely, or characteristic, dAGN luminosity ratio $(L_2/L_1)_{\rm ch}$. Figure 5 shows the distribution of $(L_2/L_1)_{\rm ch}$ for different types of sMBH orbits (including the sense of rotation and initial eccentricity) as well as for different values of $M_{\rm bin}$. Since in our models the luminosity of the pMBH is constant in time in each individual merger scenario, the differences in $(L_2/L_1)_{\rm ch}$ are driven by the changes in accretion luminosity of the sMBH.

For example, each panel illustrates that a larger $M_{\rm bin}$ is more likely to produce higher values of $(L_2/L_1)_{\rm ch}$. This is because the BHL accretion rate onto the sMBH is proportional to the local gas density, and the gas disk in our model has an exponential profile with a scale radius that depends on $\log(M_1)$. Hence, models with a larger pMBH have a gas density profile that decreases more slowly with radius and the resulting sMBH accretion rates are larger. The effects of the radial gas density

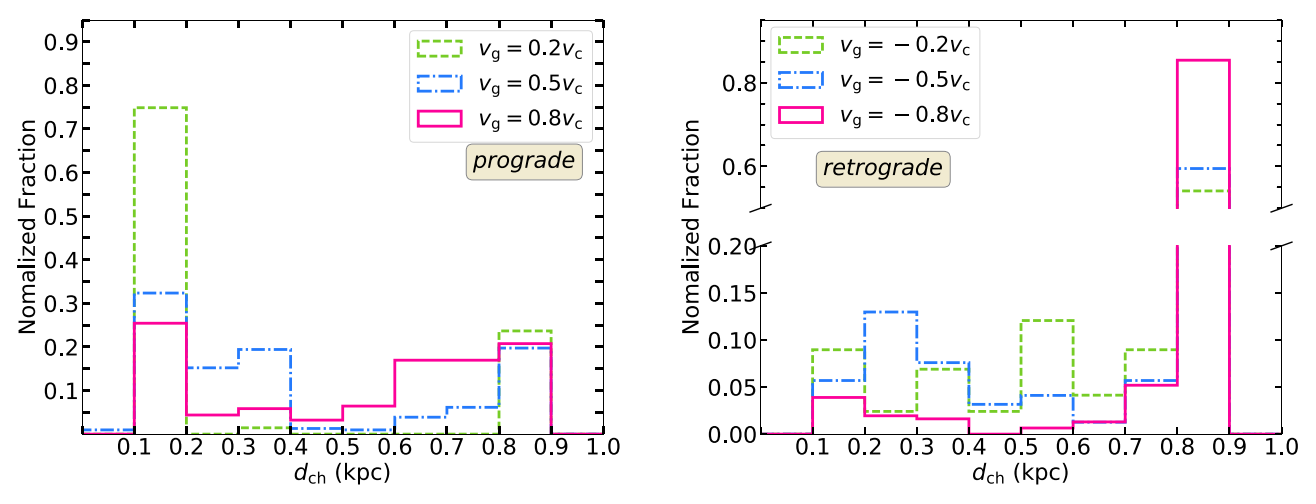


Figure 4. Histograms of the characteristic dAGN separation, d_{ch} for sMBHs on prograde (left) and retrograde (right) orbits as a function of the rotation speed of the merger remnant galaxy. Negative values of v_g indicate retrograde orbits.

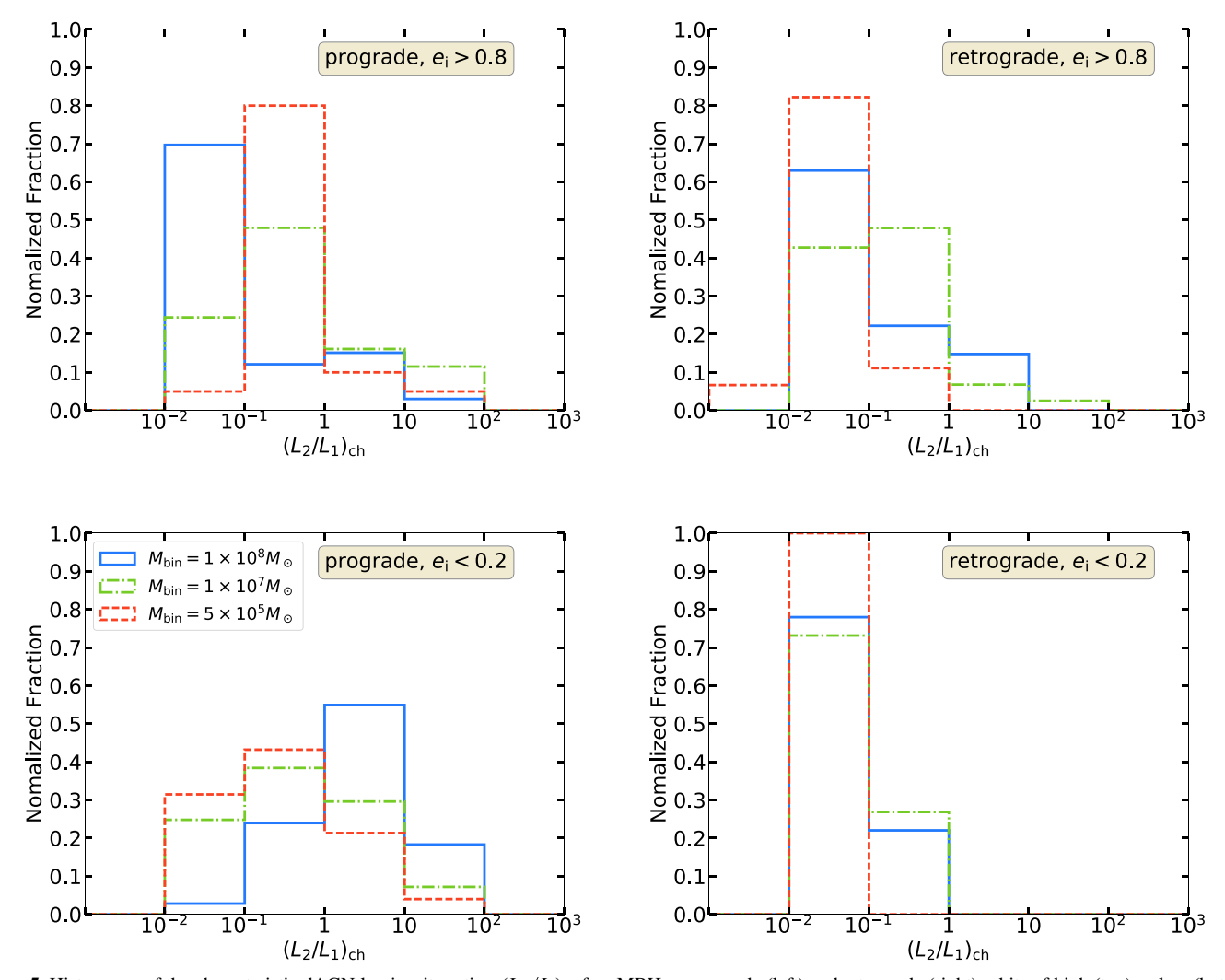


Figure 5. Histograms of the characteristic dAGN luminosity ratios, $(L_2/L_1)_{ch}$ for sMBH on prograde (left) and retrograde (right) orbits of high (top) or low (bottom) initial eccentricity. Each panel shows the distribution of $(L_2/L_1)_{ch}$ for different M_{bin} .

profile are also seen in the panels showing prograde orbits with different e_i . Very eccentric orbits bring the sMBH to the outskirts of the gas disk where the gas density is low. As a result, these dAGNs have significantly smaller $(L_2/L_1)_{\rm ch}$ compared to low e_i systems. A sMBH on a retrograde orbit

will have a large velocity relative to the gas disk (Δv) regardless of e_i , which will reduce its BHL accretion rate. As a result, $(L_2/L_1)_{\rm ch}$ values of these dAGNs are often less than 0.1.

The effects of the rotational speed of the galaxy on $(L_2/L_1)_{\rm ch}$ can be seen in Figure 6. The left panel shows that sMBHs on

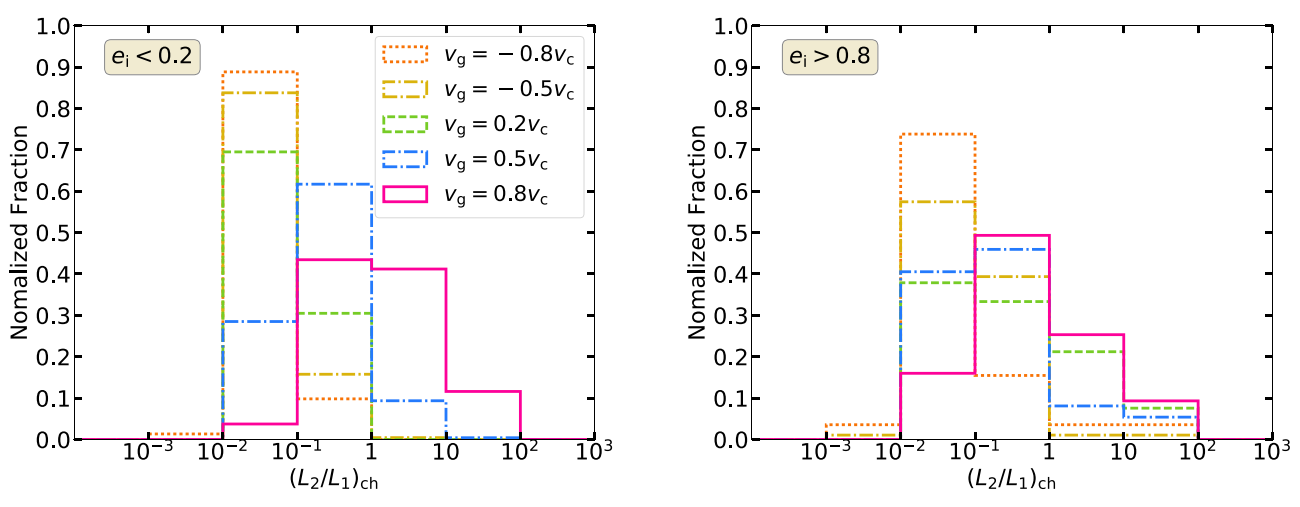


Figure 6. Histograms of the characteristic dAGN luminosity ratios, $(L_2/L_1)_{ch}$, for sMBH on orbits with low (left) and high (right) initial eccentricity. Each panel shows the distribution of $(L_2/L_1)_{ch}$ for different rotation speeds of the galactic disk. Positive (negative) values of v_g indicate sMBHs on prograde (retrograde) orbits.

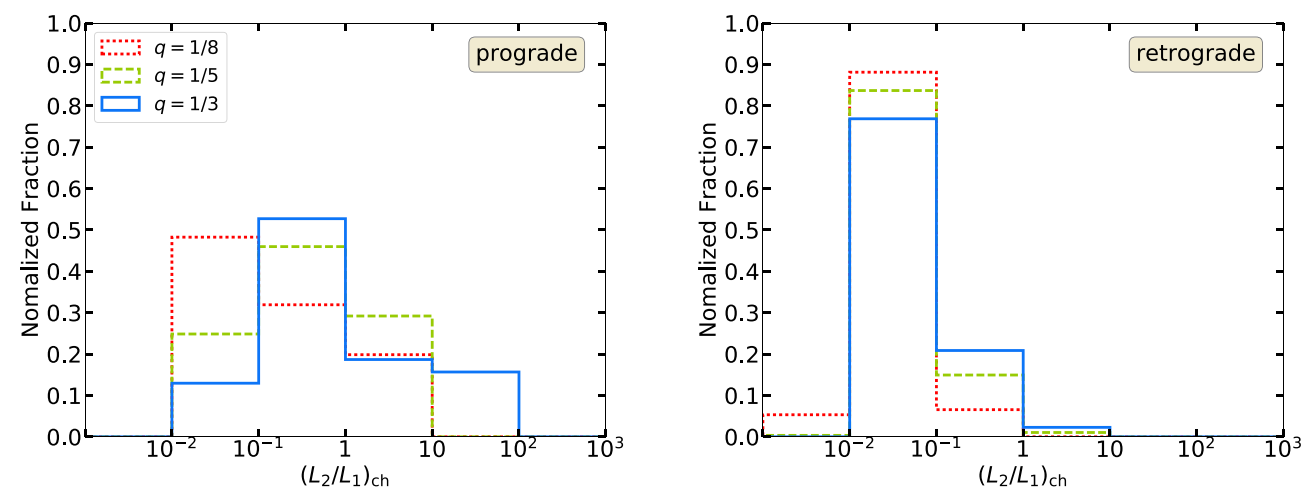


Figure 7. Histograms of the characteristic dAGN luminosity ratios, $(L_2/L_1)_{ch}$, for sMBHs on prograde (left) and retrograde (right) orbits and different values of the mass ratio, q.

orbits with low initial eccentricity have larger $(L_2/L_1)_{ch}$ values when the MBHs are co-rotating with the gas disks. This is particularly true as v_g tends to v_c . For example, nearly 80% of dAGNs in gas disks with $v_g = 0.8v_c$ have $(L_2/L_1)_{ch}$ in the range of $\sim 10^{-1}$ –10. On the other hand, 75% of dAGNs where the sMBH is on a retrograde orbit in a gas disk with $v_{\rm g}=-0.8v_{\rm c}$ have $(L_2/L_{\rm l})_{\rm ch}$ in the range of $10^{-2}\sim10^{-1}$. This effect is due to the magnitude of the relative velocity, since MBHs on circular prograde orbits have a smaller Δv , which results in a larger accretion rate onto the sMBH and a bigger $(L_2/L_1)_{ch}$. In contrast, a sMBH on a retrograde orbit will have a large Δv , suppressing the accretion rate and reducing $(L_2/L_1)_{ch}$ by orders of magnitude. Interestingly, the right panel of Figure 6 shows that Δv has a weaker effect when $e_i > 0.8$. In these cases, the sMBHs spend significant time in the outer (low density) regions of the gas disk, and are therefore most likely to be observed with a $(L_2/L_1)_{ch} < 1$, regardless of v_g .

The mass ratio of the two MBHs also impacts the distribution of $(L_2/L_1)_{\rm ch}$, as shown in Figure 7. For prograde orbits, dAGNs with larger q have larger $(L_2/L_1)_{\rm ch}$. For example, almost 60% of dAGNs with q=1/3 have $(L_2/L_1)_{\rm ch}$ in the range of $10^{-1}\sim 1$, while nearly 70% of those with q=1/8 have $(L_2/L_1)_{\rm ch}$ in the range of $10^{-2}\sim 10^{-1}$. This is

because the Bondi accretion rates on both MBHs are proportional to the square of their mass and thus, a larger mass ratio leads to a larger luminosity ratio. The right panel of Figure 7 shows that $(L_2/L_1)_{\rm ch}$ distribution of dAGNs where the sMBHs are on retrograde orbits are not strongly impacted by an increase in q. In such cases, the relative velocity between the sMBH and the gas disk is always large enough to counteract the increase in luminosity ratio caused by a higher mass ratio.

In summary, our simulations show that kiloparsec-scale dAGNs are most likely to be observed with $(L_2/L_1)_{\rm ch} < 1$ or even <0.1. More favorable luminosity ratios are however possible if the sMBH is on a prograde, low eccentricity orbit, particularly in a rapidly rotating, high mass galaxy. A larger q is also expected to increase the characteristic luminosity ratio of such dAGNs.

4.3. The Detectability of Kiloparsec-scale dAGNs

Of all systems considered in previous sections, we expect configurations that lead to long-lived, widely separated dAGNs with high luminosity ratios to be more likely to be detected. The combination of these three properties (separation, luminosity ratio, evolution timescale) therefore determines the detectability of a dAGN. As all of these properties are sensitive

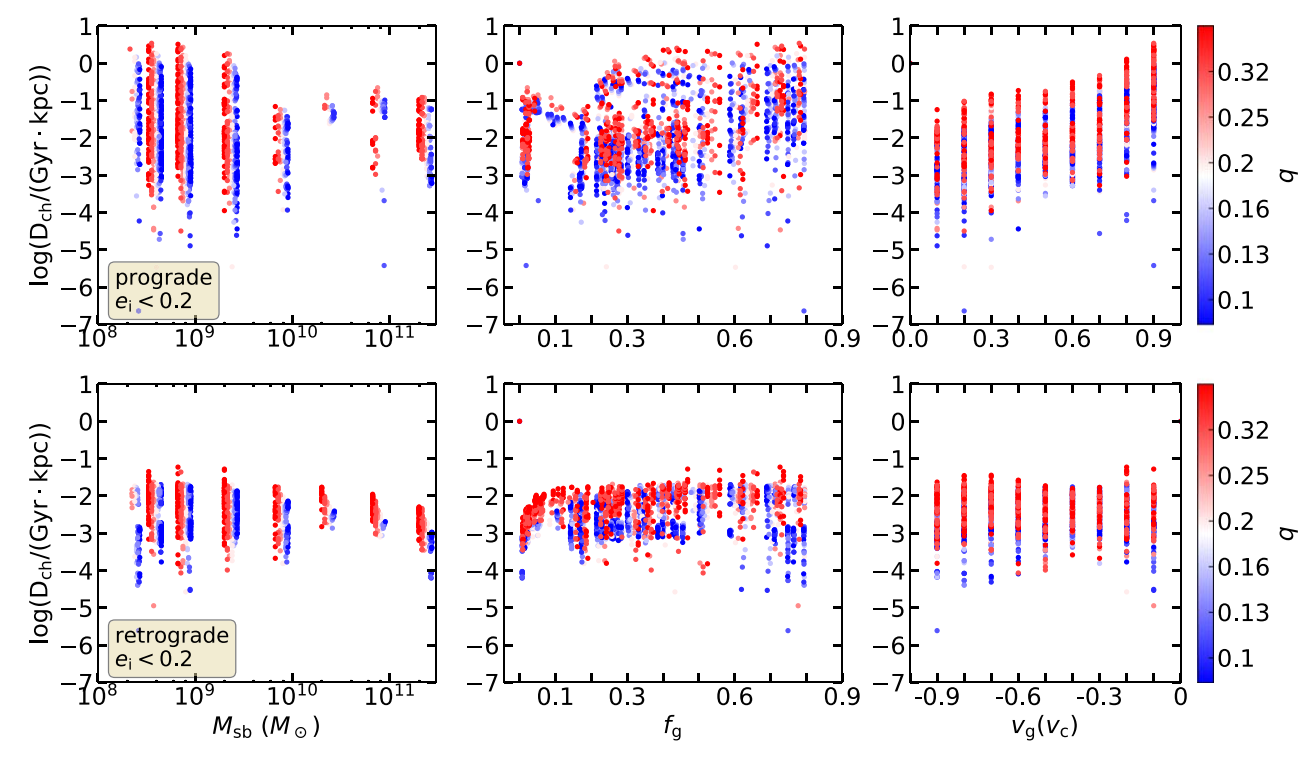


Figure 8. The detectability, D_{ch} , of kiloparsec-scale dAGNs with $e_i < 0.2$ plotted as a function of the stellar bulge mass of the merger remnant galaxy (M_{sb} ; left panels), the total gas fraction of the galaxy within 1 kpc (f_g ; middle), and the rotation speed of the galactic disk (v_g ; right). The top (bottom) panels correspond to sMBHs on prograde (retrograde) orbits. Each dot corresponds to one merger model in our suite and the color denotes the mass ratio of the pair, q. The most detectable dAGNs have sMBHs on preferentially prograde orbits and are found in gas dominated galaxies with rapidly rotating disks.

to the orbital and galactic properties, it is important to to understand what types of galaxies and orbits will lead MBH pairs that are preferentially detected as dAGNs. To address this question, we calculate the detectability, $D_{\rm ch}$, for all dAGN models in our suite:

$$D_{\rm ch} = d_{\rm ch} \times (L_2/L_1)_{\rm ch} \times f_t[d_{\rm ch}, (L_2/L_1)_{\rm ch}] \times t_{\rm evol}.$$
 (7)

That is, $D_{\rm ch}$ for is the product of the most probable separation (in kiloparsec) and luminosity ratio and separation, the fraction of the total evolution time it spends at those two values, and the total evolution time of the MBH pair (in gigayears). For any given combination of $(d_{\rm ch}, (L_2/L_1)_{\rm ch}, t_{\rm evol})$, a kiloparsec-scale dAGN is more likely to be detectable if it has a larger value of $D_{\rm obs}$.

Figures 8 and 9 show $D_{\rm ch}$ for models with low and high initial orbital eccentricity, respectively, and the subpanels illustrate the dependence on the key properties of the merger remnant galaxy. We define the total gas fraction of the model galaxy within 1 kpc, shown as a parameter in the middle panels of both figures, as

$$f_{\rm g} = \frac{M_{\rm gd,1}}{(M_{\rm gd,1} + M_{\star})},$$
 (8)

where M_{\star} is the total mass of the bulge and stellar disk within this radius.

Many of the results found in the previous section can also be identified in Figure 8. In general, dAGNs with an sMBH on a $e_i < 0.2$, prograde orbit are more detectable than retrograde ones because the sMBHs on prograde orbits are characterized by higher luminosity ratios and larger $D_{\rm ch}$ (e.g., Figure 6). Considering the prograde dAGNs more closely, we find that

those in host galaxies with small $M_{\rm sb}$, large $f_{\rm g}$, $v_{\rm g}$ close to $v_{\rm c}$, and large q are the most detectable. As discussed in Section 4.2, dAGNs with large q or dAGN in galaxies with $v_{\rm g} \approx v_{\rm c}$ are more likely to produce a higher L_2/L_1 and are therefore more easily detectable. The dAGNs in host galaxies with $M_{\rm sb} < 10^{10}\,M_{\odot}$ or $f_{\rm g} > 0.2$ are more detectable because the orbital decay in these galaxies is frequently dominated by gaseous DF. LBB20a showed that in these cases the sMBH has a longer evolution time compared to those systems where the DF due to the stellar bulge dominates the orbital evolution. The longer timescale for orbital decay means that sMBHs in these galaxies spend more time at larger separations, and are therefore more easily detectable as dAGNs.

The detectability of dAGNs with sMBHs that have $e_i > 0.8$ are shown in Figure 9. The plots indicate that eccentric and prograde dAGNs are on average slightly less detectable than their counterparts with $e_i < 0.2$. The apocenters of $e_i > 0.8$ orbits are located further out in the galactic gas disk, where the gas density is low. This makes the accretion rate of the sMBHs, the luminosity ratio, and the $D_{\rm ch}$ lower compared to those of dAGNs in host galaxies with the same properties but of low initial eccentricity.

Figure 9 also shows that when it comes to systems with $e_i > 0.8$ prograde orbits, their detectability peaks in a narrow range of bulge masses centered on $M_{\rm sb} \approx 5 \times 10^8~M_{\odot}$. The initial rise in $D_{\rm ch}$ with increasing $M_{\rm sb}$ can be understood because the accretion rate of sMBHs and the luminosity ratio are larger in more massive galaxies (see Section 4.2). However, as $M_{\rm sb}$ increases the evolution time of dAGNs shortens, which causes $D_{\rm ch}$ to reach a maximum at $M_{\rm sb} \approx 5 \times 10^8~M_{\odot}$ and then decrease. This is a reflection of the fact that in larger stellar

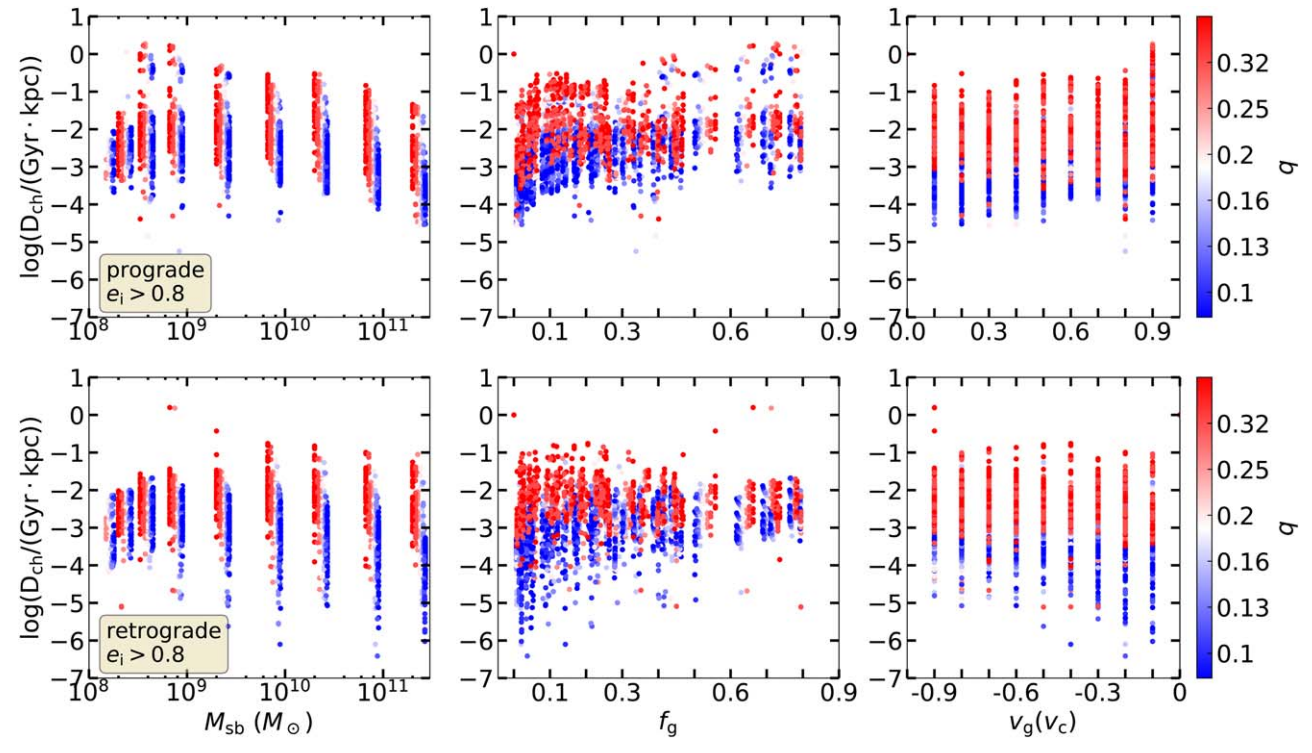


Figure 9. As Figure 8, but now showing the detectability D_{ch} for dAGNs where the sMBH is on a high initial eccentricity orbit.

bulges orbital evolution of the sMBH becomes increasingly dominated by stellar DF, and therefore faster, on average.

dAGNs on retrograde $e_i > 0.8$ orbits are more easily detectable than those on retrograde $e_i < 0.2$ orbits (see bottom rows in Figures 9 and 8). This is because the orbital velocity of a sMBH on a more eccentric retrograde orbit is smaller at the apocenter, which makes the $\Delta \nu$ smaller as well. The lower relative speed increases the efficiency of BHL accretion onto the sMBH and consequently, L_2/L_1 .

In summary, the results shown in Figures 8 and 9 indicate that dAGNs are more likely to be detected in gas-rich post-merger galaxies with rapidly rotating disks. In addition, the detectability is increased for large q and an sMBH that is on a low eccentricity prograde orbit. In contrast, dAGNs where the sMBH is on a $e_{\rm i} < 0.2$, retrograde orbit are the least detectable systems in any post-merger galaxy remnant.

4.4. The Impact of Radiation Feedback on dAGN Detectability

The radiation produced by each MBH of a dAGN can influence both the luminosity and dynamics of the system. The thermal pressure of the ionized bubble surrounding an accreting MBH regulates its accretion rate (e.g., Ostriker et al. 1976; Begelman 1985; Ricotti et al. 2008; Park & Ricotti 2011, 2012), potentially suppressing the emitted luminosity. The magnitude of this effect depends on the motion of the MBH, as well as the density and temperature of the surrounding gas (Park & Ricotti 2013). Similarly, the shape of the ionized bubble can affect the DF force for a MBH moving in a gas-rich medium (Park & Bogdanović 2017; Gruzinov et al. 2020; Toyouchi et al. 2020). Below, we investigate how these phenomena impact the predicted detectability of dAGNs.

We first consider the accretion rates and resulting luminosities of the stationary pMBH and the moving sMBH in the presence of radiative feedback. To calculate the accretion rate

onto the pMBH in the presence of radiative feedback we use the parametric model developed by Park & Ricotti (2012), calibrated on their radiation hydrodynamic simulations. Specifically, we make use of their Equations (7), (16), and (21), with a spectral index of 1.5 and radiative efficiency of 0.1. We find that the radiation feedback does not affect the accretion rate and luminosity of most pMBHs in our models, because the gas densities surrounding them are sufficiently high to counter the effect of the radiation pressure. This places most pMBHs in our model in the so-called hyper-Eddington accretion regime (Inayoshi et al. 2016), characterized by mass accretion rates larger than the Eddington rate and emergent luminosities $\lesssim L_{\rm Edd}$, limited by photon trapping in the high density gas. Hence, we limit the luminosity of the pMBHs in this regime to 10% of the Eddington luminosity.

The moving sMBH on the other hand finds itself in the regime where radiation feedback can strongly suppress its accretion rate (see Appendix). Here, we adopt the parametric model from Park & Ricotti (2013) to calculate the reduced accretion rate onto the sMBH in the presence of radiative feedback. They showed that the accretion rate onto a moving MBH increases as $\propto \Delta \nu^2$ until $\Delta \nu \approx 2c_{\rm s,in}$ (where $c_{\rm s,in} \approx 2c_{\rm s,\infty}$ is the sound speed inside the ionized region), and beyond this value asymptotes to the classical BHL solution:

$$\dot{M}_{2} \approx \frac{\rho_{\infty} (G M_{2})^{2}}{c_{s,in}^{3}} \times \begin{cases}
0.7 \left(\frac{\Delta v}{2 c_{s,in}}\right)^{2}, & 0 < \Delta v \leqslant 2 c_{s,in} \\
\times \left\{\left(1 + \left(\frac{\Delta v}{c_{s,in}}\right)^{2}\right)^{-3/2}, & \Delta v \gg 2 c_{s,in}.
\end{cases} (9)$$

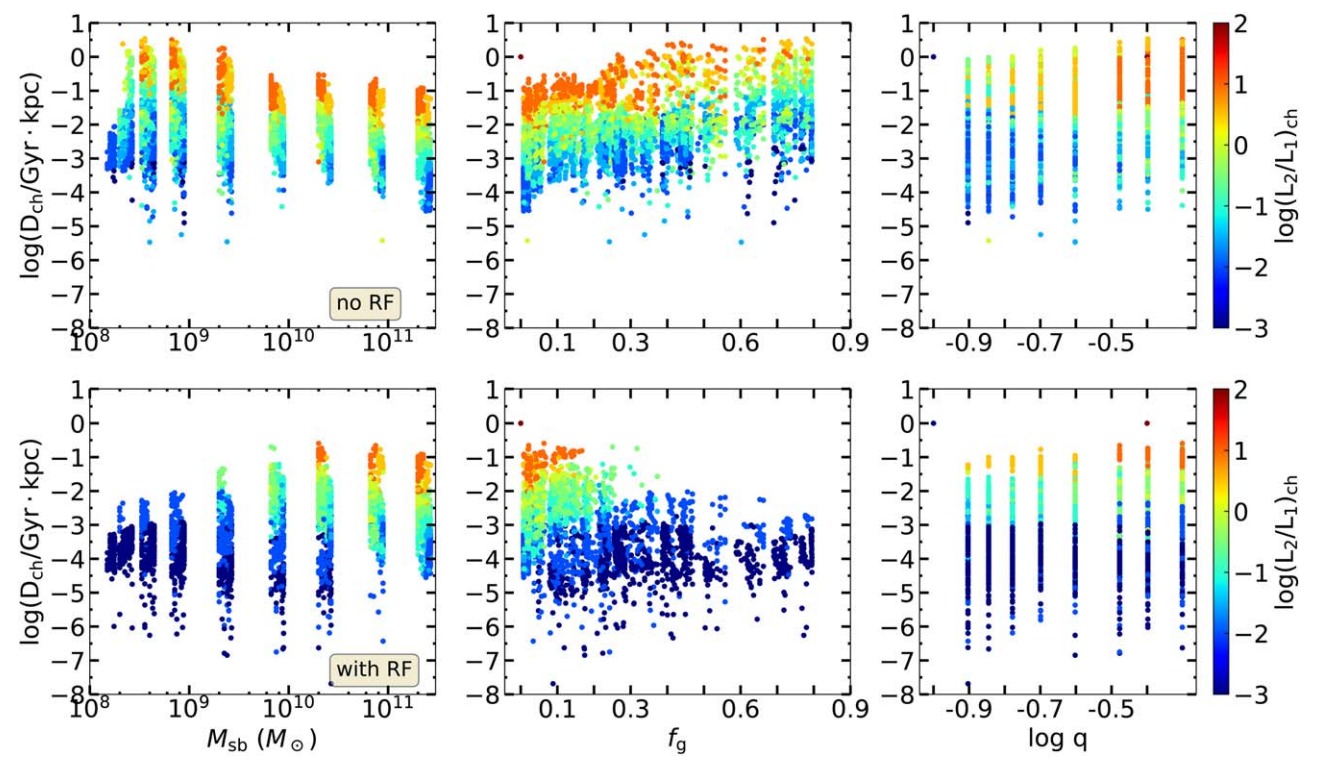


Figure 10. Detectability of dAGNs in the models without (top) or with (bottom) the radiation feedback effects. Dots represent dAGN systems on prograde orbits regardless of eccentricity and the color bar marks $(L_2/L_1)_{ch}$.

The first line of Equation (9) indicates that the accretion rate of the sMBH is significantly suppressed relative to the BHL rate when the Mach number $\mathcal{M} = \Delta v/c_{\rm s,\infty} < 5$ (where the gas temperature in the regions unaffected by the sMBH is calculated as in Section 2.2). We therefore expect the radiative feedback effects to be more prominent for sMBHs on prograde orbits, when Δv is relatively small and the Mach number remains in this range.

Radiation feedback not only affects the accretion rate but may also change how DF influences the inspiral of the sMBH—we consider this effect next. Depending on the motion of the MBH relative to the background medium, as well as the properties of the ionized gas, the shape of the gaseous wake around the MBH can reverse the direction of the DF force and speed up the moving MBH (an effect referred to as negative DF; Park & Bogdanović 2017; Gruzinov et al. 2020; Toyouchi et al. 2020). LBB20b modeled this effect and studied how negative DF changes the evolution of MBH pairs in different types of host galaxies. They find that radiation feedback leads to longer t_{evol} , and is more important in merger remnants with gas fraction $f_g > 0.1$, rotation speeds $v_{\rm g} \sim v_{\rm c}$, and when sMBHs are on prograde, low eccentricity orbits. We therefore expect radiative feedback by the sMBH to impact the detectability of some fraction of dAGNs due to these dynamical effects resulting in longer t_{evol} .

To quantify the effects of radiative feedback we reran our full dAGN model suite (described in Section 2) with parametric models described in previous paragraphs. We evaluate the detectability of each new model and compare it to models in the absence of radiation feedback in Figure 10. Since the effects of radiative feedback are strongest for sMBHs on prograde orbits, we only show $D_{\rm ch}$ for these type of systems.

The color bar of Figure 10 indicates dAGNs in models with radiative feedback show a significant drop in $(L_2/L_1)_{ch}$ caused

by the suppression of accretion onto the sMBH. Although the effects of negative DF typically increase $t_{\rm evol}$ (LBB20b), the competing decrease in $(L_2/L_1)_{\rm ch}$ completely overtakes it, resulting in a lower overall value of $D_{\rm ch}$ for dAGNs affected by radiation. Since radiative feedback is more likely to arise in gas-rich environments, the suppression of $D_{\rm ch}$ is most noticeable when the merger remnant galaxy is dominated by the gas disk (which in our models corresponds to $M_{\rm sb} < 10^{11}~M_{\odot}$ or $f_{\rm g} > 0.2$). The drop in $D_{\rm ch}$ does not have a strong relation with q however, meaning the effect of radiative feedback does not have a strong preference for the mass ratio of dAGNs.

Because the sMBH accretion rate and luminosity in the models with radiative feedback effects are a sensitive function of the relative velocity between the sMBH and the rotating gas disk in the remnant galaxy (Equation (9)), we also examine the dependence of detectability on this factor. The left panel of Figure 11 illustrates that in the absence of the radiation feedback, the dAGNs in galaxies with $v_{\rm g} \approx v_{\rm c}$ are more easily detectable because this condition leads to a larger BHL accretion rate. The right panel of Figure 11 shows that in the presence of feedback, the same group of systems has reduced detectability, due to the suppression of accretion onto the sMBH. This is because, as noted before, the drop in L_2 due to radiative feedback is most significant in the range of $0 < \mathcal{M} < 5$, which here roughly corresponds to systems with $v_{\rm g} > 0.5 v_{\rm c}$.

For simplicity, Figures 10 and 11 show the combined results for sMBHs on both low and high eccentricity orbits. It is worth noting however that the decrease in $D_{\rm ch}$ due to radiation feedback is about ~ 100 times more pronounced for low eccentricity orbits. This is because the systems with eccentric orbits exhibit lower sMBH accretion rates independent of the presence of radiation feedback effects, since they spend a significant portion of their time close to the orbital apocenter, in the region of the galaxy

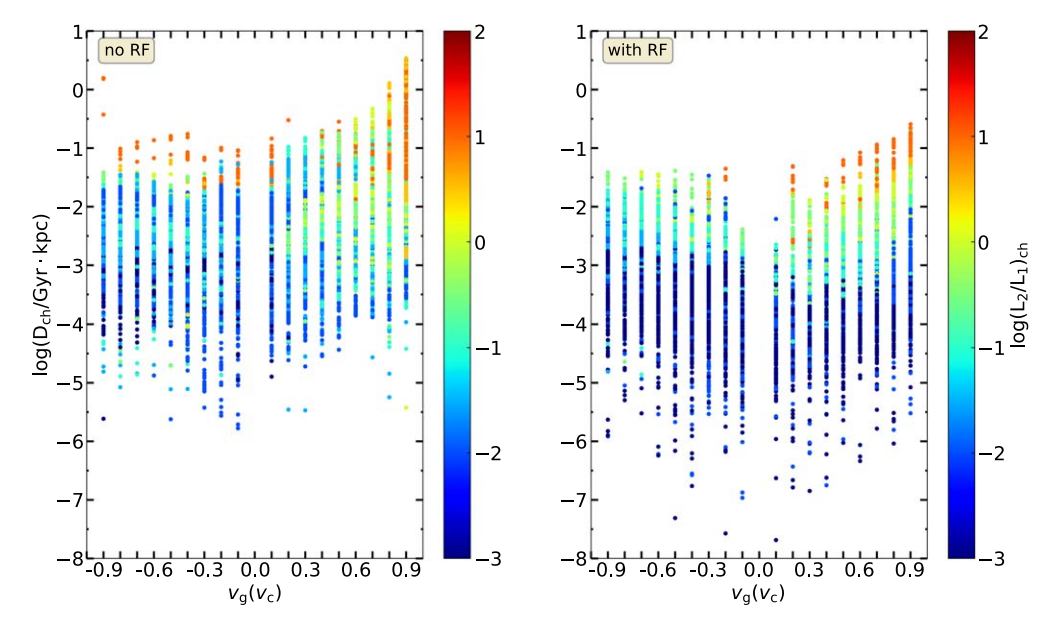


Figure 11. Detectability of dAGNs as a function of the rotation speed of the galaxy remnant in models without (left) or with (right) the radiation feedback effects. Negative (positive) values of v_g represent sMBHs on retrograde (prograde) orbits. The color bar marks $(L_2/L_1)_{ch}$.

remnant where the gas density is low. Thus, their (low) detectability is not significantly affected by radiation feedback.

In summary, dAGNs in models with radiative feedback show a significant drop in detectability caused by the suppression of accretion onto the sMBH. The suppression of detectability is most significant when the merger remnant galaxy is dominated by the gas disk ($M_{\rm sb} < 10^{11}~M_{\odot}$ or $f_{\rm g} > 0.2$) and the sMBH is on a prograde orbit within a rapidly rotating galaxy. On the other hand, the effects of radiative feedback are largely independent on the mass ratio of the MBH pair.

5. Discussion

5.1. Implications for Observations of dAGNs

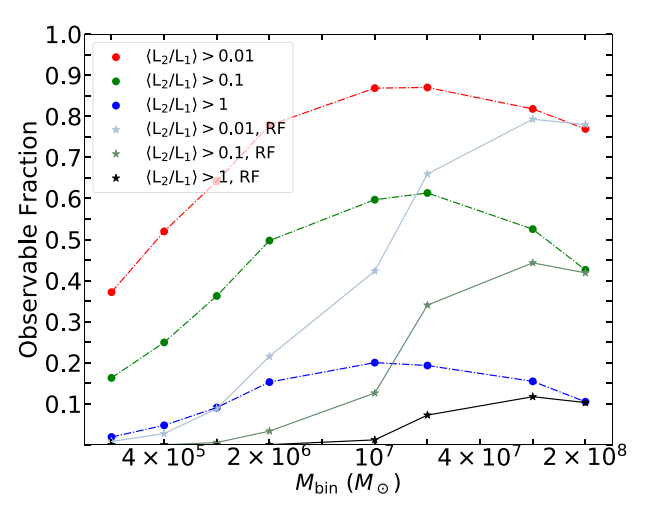
Observationally identifying sub-kiloparsec dAGNs is a daunting challenge with a relatively low number of unambiguously confirmed cases (on the order of \sim 10; De Rosa et al. 2019). dAGN candidates are often selected from catalogs of AGNs that exhibit double-peaked [O III] λ 5007 Å emission lines. However, since there are multiple plausible causes for existence of the double-peaked lines in the AGN spectra (e.g., Crenshaw et al. 2010; Rosario et al. 2010; Müller-Sánchez et al. 2015), follow-up high-resolution imaging or spatially resolved spectroscopy is needed to identify two distinct nuclear sources in the candidate host galaxy (e.g., Comerford et al. 2012; Fu et al. 2012; Hou et al. 2019, 2020; Foord et al. 2020). This is an observationally expensive strategy to identify dAGNs and the results in this work can provide guidance on how to best prioritize follow-up observations of candidate dAGNs.

The most important property of the host galaxies that enhances the detectability of dAGNs is the rotation speed, v_g . If the sMBH is on a prograde orbit, then it is more likely to spend a large fraction of its orbit with a low Δv , boosting its luminosity (e.g., Figures 6, 8, and 9). Similarly, if the eccentricity of the orbit remains moderately low, then the evolution of the orbit can be slow enough that there is a good chance that the dAGN will be observed at a separation of ~ 0.7 –0.8 pc (Figure 4).

The size and relative mass of the gas disk in the candidate galaxy is another important element in determining the detectability of dAGNs. The orbital decay of the sMBH speeds up once it enters the stellar bulge, so galaxies with either small bulges or massive gas disks are be easier to detect as dAGNs, as the sMBH will be more likely to be observed at larger separations. A larger gas fraction of the galaxy should nominally also increase the detectability of dAGNs by enhancing the likelihood of rapid accretion onto the sMBH. However, as shown in Figure 10, radiation feedback effects are also most important in galaxies with large f_g , and could significantly decrease the detectability by suppressing accretion onto the sMBH. If the radiation feedback effects indeed act as described in Section 4.4, then large, relatively gas-poor galaxies are the best candidates for detecting dAGNs. In this case, the rapid evolution of the sMBH in the large bulge is compensated by the overall increase in the characteristic separation of the system (e.g., Figure 3).

Our results also indicate that identified sub-kiloparsec dAGNs will most likely have large q with a sMBH on a prograde orbit. As shown in Figures 8 and 9, significantly more low e_i models yield high $D_{\rm ch}$ than high e_i ones. Therefore, it is likely that detected dAGNs will contain sMBHs on low eccentricity orbits.

Another demonstration of the challenges and trade-offs of observationally searching for dAGNs is shown in Figure 12. Figure 12 illustrates the observable fraction of dAGNs which is defined as the fraction of dAGNs whose time-averaged luminosity ratio ($\langle L_2/L_1 \rangle$) throughout the evolution process is larger than a threshold value. In the absence of radiation feedback, dAGNs of $M_{\rm bin} \sim 10^7~M_{\odot}$ have the highest observable fraction in our simulations (left panel of Figure 12). Nearly 90% of these dAGNs are observable if setting $\langle L_2/L_1 \rangle > 0.01$ to be the limit. As the pair mass increases, the observable fraction of dAGNs first increases then turns over. The rise is due to the increasing disk scale radius, which leads to a slower gas density drop and results in a higher mean luminosity ratio. While the turn over is because of the fast evolution rate inside the bulge which reduces the time these



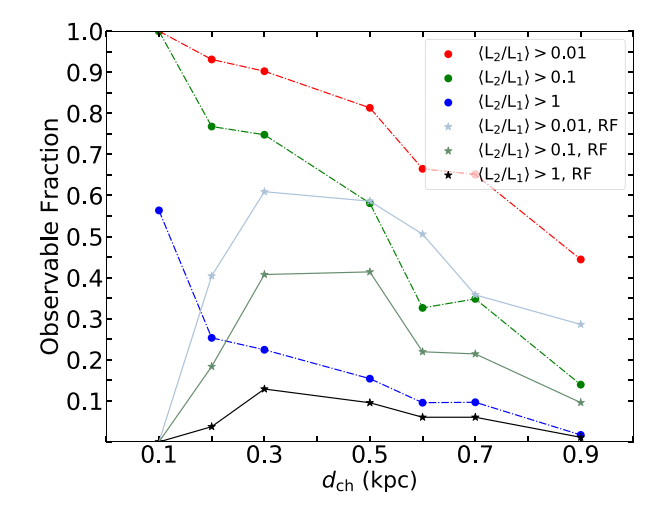


Figure 12. Fraction of dAGNs that can be observed above time-averaged luminosity ratio ($\langle L_2/L_1 \rangle$) of 0.01, 0.1, and 1 at different pair mass (left) and characteristic separation (right).

dAGNs shine with high luminosity ratio. However, including radiation feedback drops the observable fraction to 40% assuming the same limit. On the other hand, the observable fraction of dAGNs with $M_{\rm bin} \sim 2 \times 10^8 \, M_{\odot}$ is larger than 75% and only weakly affected by radiation feedback effects since these models have very large bulges and low gas fractions which make the gas based radiation feedback effect negligible. Thus, we expect dAGNs with higher pair mass to have a higher observable fraction in observational surveys of dAGNs.

Almost all dAGNs with characteristic separations smaller than 0.3 kpc have $\langle L_2/L_1\rangle$ above 0.01 (right panel of Figure 12). The curves rise to low separation because as the separation becomes smaller, the gas density becomes larger increasing both the luminosity ratio and the observable fraction. However, the suppression of accretion onto the sMBH due to radiation feedback is predicted to significantly suppress the observable fraction at small separations. Thus, after accounting for the impact of radiation feedback, separations of \sim 0.3–0.5 kpc will lead to the highest observable fractions of dAGNs.

5.2. Impact of Simplifying Assumptions

The advantage of our semi-analytic model is the ability to run simulations over a wide range of galaxy and orbital properties at the cost of making some simplifying assumptions. The potential impact of our assumptions on the dynamical aspects of evolution of MBH pairs is discussed in LBB20a and LBB20b. Here, we consider the possible effects of these assumptions on the derived dAGN properties.

We assume the pMBH is fixed at the center of the host galaxy. If the motion of the pMBH and its orbital decay due to DF forces are included in the simulations, the resulting $t_{\rm evol}$ would be shorter, thus reducing $D_{\rm ch}$. This effect would be strongest in comparable mass MBH pairs and weaker in those with small q. However, if the pMBH is moving, it would accrete at the BHL rate, which is smaller than the Bondi rate used in the current model, increasing L_2/L_1 and the detectability. Again, this effect would be stronger for comparable mass MBH pairs, since Δv of the pMBH would be maximized in this case. As the these two effects compete against each other, we do not expect a large systematic discrepancy in $D_{\rm ch}$ due to this assumption.

Similarly, the orbit of the sMBH is assumed to always reside in the midplane of the galaxy. If inclined orbits take the sMBH outside of the gas disk, $t_{\rm evol}$ will increase since the gaseous DF force would be less efficient. For highly inclined orbits, however, the sMBH will spend a large fraction of time in the low gas density regions and the characteristic luminosity ratio, $(L_2/L_1)_{\rm ch}$, would likely be many orders of magnitude smaller relative to a sMBH on a coplanar orbit. This effect is likely to overtake the increase in $t_{\rm evol}$ and we therefore expect the detectability of dAGNs where the sMBH is on an inclined orbit to be much smaller than for the coplanar systems.

The masses of the two MBHs in the models are held fixed during our calculations. If we allow the MBHs to gain mass, we find that the average change in q is \lesssim 60%. By assuming a fixed mass ratio throughout the evolution, we provide a lower limit of the detectability. If the growth of mass of MBHs by accretion is taken into account, we expect the detectability to increase by less than an order of magnitude independent of the presence of radiation feedback. In the context of Figures 8 and 9, we expect the distribution shifts toward larger $M_{\rm tot}$, smaller $f_{\rm g}$, and larger detectability due to the increased mass ratio in the evolution.

6. Conclusions

We present the results of nearly 40,000 simulations of model dAGN systems, in which we follow the orbital evolution of the sMBH as it decays in response to the DF forces from the gas and stellar components of the merger remnant galaxy. For each dAGN, we calculate how orbital separation and luminosity ratio of the two MBHs change as a function of the properties of the galaxy and sMBH orbit and use them to evaluate the most probable separations, $d_{\rm ch}$, and luminosity ratios, $(L_2/L_1)_{\rm ch}$. Together with the evolution timescale, $t_{\rm evol}$, we use these properties to define the detectability and gauge which systems are most likely to be discovered as dAGNs in observations. We find that:

- 1. The low, unequal mass MBH pairs (e.g., $M_{\rm bin}=3\times 10^6\,M_{\odot}$, q=1/9) in slowly rotating galaxies have most probable dAGN luminosity ratios of $\sim 10^{-2}$ and the most probable dAGN separations $d\sim 0.3-0.4$ kpc for prograde and $\sim 0.4-0.9$ kpc for retrograde orbits (see Section 3).
- 2. The high, comparable mass MBH pairs (e.g., $M_{\rm bin} = 10^8 \, M_{\odot}$, q = 1/3) in rapidly rotating galaxies on the other hand exhibit higher characteristic dAGN luminosity ratios and separations. The latter is a consequence of a relatively slow evolution of these systems at large

- separations, where they spend a significant fraction of their overall evolution time (Section 3).
- 3. The most likely dAGN separations can be as low as ~0.1 kpc in prograde systems (especially in slowly rotating, low mass galaxies), whereas the characteristic dAGN separations for retrograde systems are ~0.8 kpc for a wide range of remnant galaxy properties (Section 4.1).
- 4. The kiloparsec-scale dAGNs are most likely to be observed with $(L_2/L_1)_{\rm ch} < 1$ or even < 0.1. Of these, systems with larger MBH mass ratios in rapidly rotating, high mass galaxies tend to occupy the higher end of the luminosity ratio distribution (Section 4.2).
- 5. Overall, dAGNs are more likely to be detected in gas-rich post-merger galaxies with rapidly rotating disks. In addition, the detectability is increased in systems with comparable MBH mass ratios characterized by low eccentricity, prograde orbits. In contrast, dAGNs on retrograde, low eccentricity orbits are some of the least detectable systems among our models (Section 4.3).
- 6. The above findings are formulated for systems in which the accreting MBHs do not exhibit radiative feedback. dAGNs in models with radiative feedback show a significant drop in $(L_2/L_1)_{\rm ch}$ caused by the suppression of accretion onto the sMBH, resulting in a lower overall detectability. Since radiation feedback is more likely to arise in gas-rich environments, the suppression in detectability is most pronounced in merger remnant galaxies dominated by the gas disk. Hence, if the radiation feedback effects operate as described here, then large, relatively gas-poor galaxies are the best candidates for detecting dAGNs (Section 4.4).

In the next decade, new X-ray observatories (e.g., extended ROentgen Survey with an Imaging Telescope Array (eROSITA), Merloni et al. 2012; Advanced Telescope for High Energy Astrophysics (Athena), Nandra et al. 2013), radio surveys (e.g., the next-generation Very Large Array (ngVLA), McKinnon et al. 2019; Square Kilometre Array (SKA); Prandoni & Seymour 2015), and optical surveys (e.g., James Webb Space Telescope, Gardner et al. 2006) will dramatically increase the population of known dAGNs, especially at separations less than or approximately equal kiloparsecs. The detectabilities computed from our models provide a convenient way to select dAGN candidates for follow-up observations. In the future, comparing a sample of kiloparsec-scale dAGNs luminosities and separations to these results will provide a test of the nature and efficiency of DF forces in transporting MBHs in post-merger galaxies.

T.B. acknowledges the support by the National Aeronautics and Space Administration (NASA) under award No. 80NSSC19K0319 and by the National Science Foundation (NSF) under award No. 1908042. We also acknowledge our anonymous referee for helpful comments.

Appendix The Distribution of Time-averaged Accretion Rates onto the MBHs

Without radiation feedback the distribution of the time-averaged accretion rates onto the sMBHs peaks sharply at an Eddington ratio of $10^{-0.5}$ with a median of $10^{-1.8}$ (Figure 13). The time-averaged accretion rate onto the pMBHs is tightly clustered around the upper limit of 10^{-1} Eddington

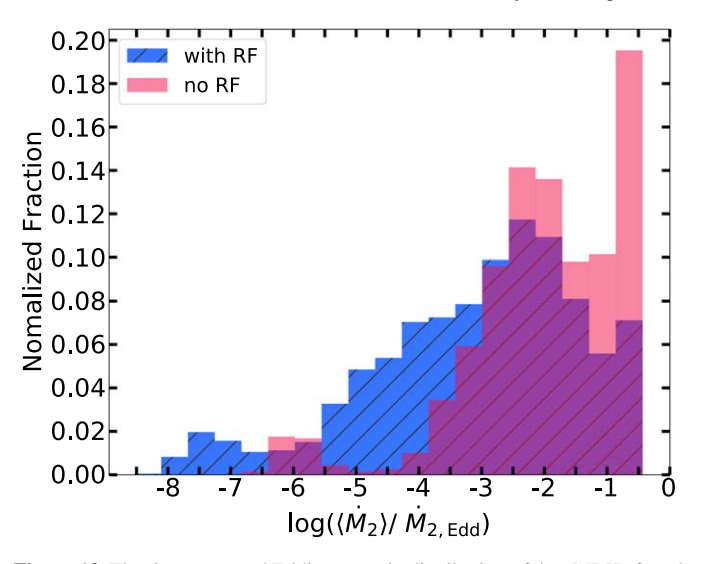


Figure 13. The time-averaged Eddington ratio distribution of the sMBHs found in the calculations with and without the effects of radiation feedback.

(Equation (1)) with a median Eddington ratio of 10^{-1} . After including the effects of radiation feedback, the sMBHs have a time-averaged accretion rate distribution that peaks at an Eddington ratio of $10^{-2.5}$ with a median of $10^{-2.7}$ (Figure 13). The accretion rate distribution of pMBHs is almost unchanged with radiation feedback.

ORCID iDs

Kunyang Li https://orcid.org/0000-0002-0867-8946 David R. Ballantyne https://orcid.org/0000-0001-8128-6976 Tamara Bogdanović https://orcid.org/0000-0002-

7835-7814

References

Amaro-Seoane, P., Audley, H., Babak, S., et al. 2017, arXiv:1702.00786 Antonini, F., & Merritt, D. 2012, ApJ, 745, 83 Barnes, J. E., & Hernquist, L. E. 1991, ApJL, 370, L65 Begelman, M. C. 1985, ApJ, 297, 492 Begelman, M. C., Blandford, R. D., & Rees, M. J. 1980, Natur, 287, 307 Binney, J., & Tremaine, S. 2008, Galactic Dynamics: Second Edition (Princeton, NJ: Princeton Univ. Press) Bondi, H. 1952, MNRAS, 112, 195 Bondi, H., & Hoyle, F. 1944, MNRAS, 104, 273 Burke-Spolaor, S. 2011, MNRAS, 410, 2113 Capelo, P. R., Dotti, M., Volonteri, M., et al. 2017, MNRAS, 469, 4437 Comerford, J. M., Gerke, B. F., Stern, D., et al. 2012, ApJ, 753, 42 Crenshaw, D. M., Schmitt, H. R., Kraemer, S. B., Mushotzky, R. F., & Dunn, J. P. 2010, ApJ, 708, 419 De Rosa, A., Vignali, C., Bogdanović, T., et al. 2019, NewAR, 86, 101525 Di Matteo, T., Springel, V., & Hernquist, L. 2005, Natur, 433, 604 Foord, A., Gültekin, K., Nevin, R., et al. 2020, ApJ, 892, 29 Foord, A., Gültekin, K., Reynolds, M. T., et al. 2019, ApJ, 877, 17 Fu, H., Myers, A. D., Djorgovski, S. G., et al. 2015a, ApJ, 799, 72 Fu, H., Wrobel, J. M., Myers, A. D., Djorgovski, S. G., & Yan, L. 2015b, , 815, L6 Fu, H., Yan, L., Myers, A. D., et al. 2012, ApJ, 745, 67 Gardner, J. P., Mather, J. C., Clampin, M., et al. 2006, SSRv, 123, 485 Gross, A. C., Fu, H., Myers, A. D., Wrobel, J. M., & Djorgovski, S. G. 2019, ApJ, 883, 50 Gruzinov, A., Levin, Y., & Matzner, C. D. 2020, MNRAS, 492, 2755 Hopkins, P. F., Hayward, C. C., Narayanan, D., & Hernquist, L. 2012, NRAS, 420, 320

Hopkins, P. F., Hernquist, L., Cox, T. J., et al. 2005a, ApJ, 630, 705

Hou, M., Li, Z., & Liu, X. 2020, ApJ, 900, 79

Hopkins, P. F., Hernquist, L., Martini, P., et al. 2005b, ApJL, 625, L71

```
Hou, M., Liu, X., Guo, H., et al. 2019, ApJ, 882, 41
Hoyle, F., & Lyttleton, R. A. 1939, PCPS, 35, 405
Inayoshi, K., Haiman, Z., & Ostriker, J. P. 2016, MNRAS, 459, 3738
Kelley, L., Charisi, M., Burke-Spolaor, S., et al. 2019, BAAS, 51, 490
Kelley, L. Z., Blecha, L., & Hernquist, L. 2017, MNRAS, 464, 3131
Kim, H., & Kim, W.-T. 2007, ApJ, 665, 432
Kormendy, J., & Ho, L. C. 2013, ARA&A, 51, 511
Koss, M., Mushotzky, R., Treister, E., et al. 2012, ApJL, 746, L22
Li, K., Bogdanović, T., & Ballantyne, D. R. 2020a, ApJ, 896, 113
Li, K., Bogdanović, T., & Ballantyne, D. R. 2020b, ApJ, 905, 123
Lusso, E., Comastri, A., Simmons, B. D., et al. 2012, MNRAS, 425, 623
Magorrian, J., Tremaine, S., Richstone, D., et al. 1998, AJ, 115, 2285
McKinnon, M., Beasley, A., Murphy, E., et al. 2019, BAAS, 51, 81
Merloni, A., Predehl, P., Becker, W., et al. 2012, arXiv:1209.3114
Mezcua, M., Lobanov, A. P., Mediavilla, E., & Karouzos, M. 2014, ApJ,
   784, 16
Müller-Sánchez, F., Comerford, J. M., Nevin, R., et al. 2015, ApJ, 813,
Nandra, K., Barret, D., Barcons, X., et al. 2013, arXiv:1306.2307
Narayanan, D., Cox, T. J., Robertson, B., et al. 2008, in ASP Conf. Ser. 381,
   Infrared Diagnostics of Galaxy Evolution, ed. R. R. Chary, H. I. Teplitz, &
   K. Sheth (San Francisco, CA: ASP), 491
Ostriker, E. C. 1999, ApJ, 513, 252
Ostriker, J. P., McCray, R., Weaver, R., & Yahil, A. 1976, ApJL, 208, L61
```

```
Park, K., & Bogdanović, T. 2017, ApJ, 838, 103
Park, K., & Ricotti, M. 2011, ApJ, 739, 2
Park, K., & Ricotti, M. 2012, ApJ, 747, 9
Park, K., & Ricotti, M. 2013, ApJ, 767, 163
Prandoni, I., & Seymour, N. 2015, in Advancing Astrophysics with the Square
   Kilometre Array (AASKA14) (Trieste: PoS), 67
Ricotti, M., Ostriker, J. P., & Mack, K. J. 2008, ApJ, 680, 829
Rosario, D. J., Shields, G. A., Taylor, G. B., Salviand er, S., & Smith, K. L.
  2010, ApJ, 716, 131
Rosas-Guevara, Y. M., Bower, R. G., McAlpine, S., Bonoli, S., &
  Tissera, P. B. 2019, MNRAS, 483, 2712
Sargent, A. I., Sanders, D. B., & Phillips, T. G. 1989, ApJL, 346, L9
Sargent, A. I., Sanders, D. B., Scoville, N. Z., & Soifer, B. T. 1987, ApJL,
  312, L35
Scoville, N. Z., Sanders, D. B., Sargent, A. I., et al. 1986, ApJL, 311, L47
Severgnini, P., Braito, V., Cicone, C., et al. 2021, A&A, 646, A153
Springel, V., Di Matteo, T., & Hernquist, L. 2005, MNRAS, 361, 776
Teng, S. H., Schawinski, K., Urry, C. M., et al. 2012, ApJ, 753, 165
Toomre, A. 1964, ApJ, 139, 1217
Toyouchi, D., Hosokawa, T., Sugimura, K., & Kuiper, R. 2020, MNRAS,
  496, 1909
Van Wassenhove, S., Volonteri, M., Mayer, L., et al. 2012, ApJL, 748, L7
White, S. D. M., & Frenk, C. S. 1991, ApJ, 379, 52
White, S. D. M., & Rees, M. J. 1978, MNRAS, 183, 341
```